The Excited-State Structure, Vibrations, Lifetimes and Nonradiative Dynamics of Jet-Cooled 1-Methylcytosine

Maria A. Trachsel,[1] Timo Wiedmer,[1] Susan Blaser,[1] Hans-Martin Frey,[1] Quansong Li,[2] Sergi Ruiz-Barragan,[3] Lluís Blancafort,[4, *] and Samuel Leutwyler[1, †]

[1]*Department of Chemistry and Biochemistry,*

University of Bern, Freiestrasse 3, CH-3012 Bern, Switzerland

[2]*Key Laboratory of Cluster Science of Ministry of Education,*

School of Chemistry, Beijing Institute of Technology, 100081 Beijing, China

[3]*Lehrstuhl für Theoretische Chemie, Ruhr-Universitat Bochum, 44780 Bochum, Germany*

[4]*Institut de Química Computacional i Catàlisi and Departament de Química,*

Universitat de Girona, Facultat de Ciències,

C/ M. Aurèlia Campmany 69, 17003 Girona, Spain

(Dated: September 16, 2016)

Abstract

We have investigated the $S_0 \rightarrow S_1$ UV vibronic spectrum and time-resolved S_1 state dynamics of jet-cooled amino-keto 1-methylcytosine (1MCyt) using two-color resonant two-photon ionization, UV/UV holeburning and depletion spectroscopies, as well as nanosecond and picosecond time-resolved pump/delayed ionization measurements. The experimental study is complemented with SCS-CC2 and MS-CASPT2 *ab initio* calculations. Above the weak electronic origin of 1MCyt at $31852 \, \text{cm}^{-1}$ about 20 intense vibronic bands are observed. These are interpreted as methyl group torsional transitions coupled to out-of-plane ring vibrations, in agreement with the methyl group rotation and out-of-plane distortions upon $^1\pi\pi^*$ excitation predicted by the calculations. The methyl torsion and ν_1' (butterfly) vibrations are strongly coupled, in the S_1 state. The $S_0 \rightarrow S_1$ vibronic spectrum breaks off at a vibrational excess energy $E_{exc} \sim 500 \, \text{cm}^{-1}$, indicating that a barrier in front of the ethylene-type $S_1 \rightsquigarrow S_0$ conical intersection is exceeded, which is calculated to lie at $E_{exc} = 366 \, \text{cm}^{-1}$. The $S_1 \rightsquigarrow S_0$ internal conversion rate constant increases from $k_{IC} = 2 \cdot 10^9 \, \text{s}^{-1}$ near the $S_1(v = 0)$ level to $1 \cdot 10^{11} \, \text{s}^{-1}$ at $E_{exc} = 516 \, \text{cm}^{-1}$. The $^1\pi\pi^*$ state of 1MCyt also relaxes into the lower-lying triplet T_1 ($^3\pi\pi^*$) state by intersystem crossing (ISC); the calculated spin-orbit coupling (SOC) value is $2.4 \, \text{cm}^{-1}$. The ISC rate constant is $10 - 100$ times lower than k_{IC}; it increases from $k_{ISC} = 2 \cdot 10^8 \, \text{s}^{-1}$ near $S_1(v = 0)$ to $k_{ISC} = 2 \cdot 10^9 \, \text{s}^{-1}$ at $E_{exc} = 516 \, \text{cm}^{-1}$. The T_1 state energy is determined from the onset of the time-delayed photoionization efficiency curve as $25600 \pm 500 \, \text{cm}^{-1}$. The T_2 ($^3n\pi^*$) state lies $> 1500 \, \text{cm}^{-1}$ above $S_1(v = 0)$, so $S_1 \rightsquigarrow T_2$ ISC cannot occur, despite the large SOC parameter of $10.6 \, \text{cm}^{-1}$. An upper limit to the adiabatic ionization energy of 1MCyt is determined as 8.41 ± 0.02 eV. Compared to cytosine, methyl substitution at N1 lowers the adiabatic ionization energy by ≥ 0.32 eV and leads to a much higher density of vibronic bands in the $S_0 \rightarrow S_1$ spectrum. The effect of methylation on the radiationless decay to S_0 and ISC to T_1 is small, as shown by the similar break-off of the spectrum and the similar computed mechanisms.

I. INTRODUCTION

In DNA, cytosine (Cyt) occurs in the form of 2'-deoxycytidine, in which deoxyribose is bound to the Cyt N1 atom. In the gas phase, however, the most stable forms of unsubstituted cytosine are the cis- and trans-enol-amino tautomers.[1–8] In 1-methylcytosine (1MCyt) the substitution of a methyl group at N1 eliminates these enol-amino forms and renders the amino-keto tautomer **1**, see Figure 1, as the most stable form, thereby providing a better mimic for cytidine. De Vries and co-workers have measured the resonant two-photon ionization (R2PI) spectrum of 1MCyt with an electronic origin at 31908 cm^{-1} followed by several vibronic bands and assigned it to the $S_0 \rightarrow S_1$ transition of the amino-keto tautomer **1**.[9,10]
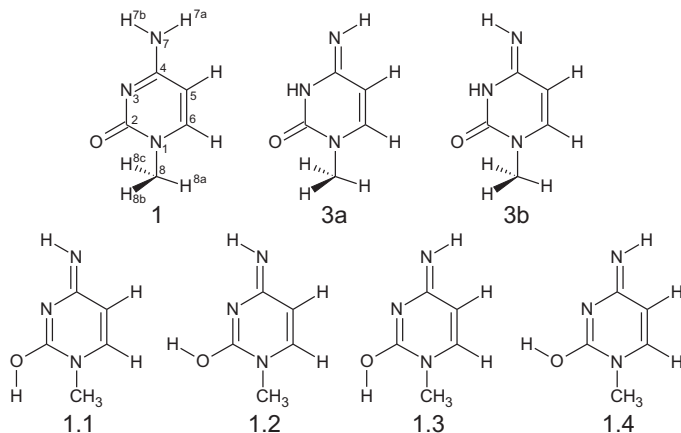
FIG. 1. The seven tautomers and rotamers of 1MCyt.

The photophysics of Cyt and its derivatives in the gas phase has been widely studied. When using fs pump/ionization techniques with excitation at $250 - 267$ nm, excited-state transients have been measured that exhibit mono-, bi-, or tri-exponential lifetimes ranging from $\tau = 50$ fs to 3.8 ps, depending on the experimental setup.[11–14] For Cyt, slower decay components of $\tau = 19$ ps and 55 ps have been also observed after excitation at longer wavelengths of 270 and 280 nm, respectively.[13,14] In the red wing of the spectrum, excitation at 290 nm gives rise to a component with a lifetime of ≥ 150 ps.[13] Lobsiger et al. determined a lower limit to the lifetime of the Cyt $S_1; v = 0$ level as $\tau = 45$ ps by modeling the Lorentzian broadening of the rovibronic band contours in the R2PI spectrum.[8] Using ps pump/ionization techniques, Blaser et al. have recently measured the lifetime at the Cyt S_1 0_0^0 band as $\tau = 730$ ps.[15] In the R2PI spectra, the short lifetimes are reflected in a break-off of the sharp vibronic bands at vibrational excess energies $E_{exc} \sim 500$ cm^{-1} above the 0_0^0 transition.[8–10]

When exciting Cyt at its 0_0^0 band (313 nm, 31900 cm^{-1}) followed by ionization at 157 nm, an excited-state signal with a lifetime of ~ 270 ns is also observed; this signal has been attributed to a triplet state.[9,10] Via the measurement of the singlet and triplet state ionization energies,

this state has been identified as the T_1 state.[16] More recently, the intersystem crossing (ISC) quantum yield and ISC rates of Cyt have been measured as a function of the S_1 state vibrational energy.[17] A long-lived excited state with a lifetime of several hundred ns has also been observed for 1MCyt following excitation near the 0_0^0 band and ionization at 157 nm.[9]

The interest in the photophysics of Cyt has motivated many theoretical studies, whose main aims were to explain the ultrashort excited-state lifetimes and the formation of the long-lived triplet state.[18–34] Most studies have considered the amino-keto tautomer. Among the points of debate is whether the structure of the S_1 minimum of $(\pi\pi*)$ character, $^1(\pi\pi)*_{Min}$, has a quasi-planar or ring-puckered conformation, for a recent discussion see ref. 34. The ultrafast decay to the ground state has been explained by the presence of conical intersections (CI) between the singlet ground and first excited states. Three different CI structures are accessible, depending on the experimental excitation energies: The lowest-energy one, called $(Eth)_X$, is characterized by an out-of-plane twist of the C_5-C_6 double bond, similar to the CI structure of ethylene.[21–26,30–32] The second CI, called $(OP)_X$, has a puckered N_3 atom and the amino group bent out of the plane.[18,24–26,30,32] The third structure, $(n_O\pi^*)_X$, has a semi-planar ring and a stretched C_2-O_7 bond.[18,24–26,30,32] The predicted decay mechanism of Cyt depends strongly on the level of theory, as discussed extensively in the literature. With methods that include dynamic correlation, such as complete active space second order perturbation (CASPT2), multi-reference configuration interaction (MRCI) and density functional theory (DFT) combined with MRCI (DFT/MRCI), the energetically favored path is associated with $(Eth)_X$. It goes through a minimum on S_1, $^1(\pi\pi)*_{Min}$, and leads to the intersection through a barrier. The estimated barrier heights are $900 \, \text{cm}^{-1}$ with MRCI[25] and CASPT2//CASSCF (CASPT2 energies calculated along a CASSCF optimized path),[24] and $645 \, \text{cm}^{-1}$ at the multistate CASPT2 (MS-CASPT2) level (geometries optimized at the same level of theory).[32] The barrier to access $(OP)_X$ from $^1(\pi,\pi)*_{Min}$ is $1050 \, \text{cm}^{-1}$ at the MRCI level,[25] $970 \, \text{cm}^{-1}$ at the CASPT2//CASSCF level[24] and $890 \, \text{cm}^{-1}$ with MS-CASPT2.[32] The energy of $(n_O\pi^*)_X$ at the CASPT2//CASSCF and MS-CASPT2 levels of theory is more than $8400 \, \text{cm}^{-1}$ above $^1(\pi,\pi)*_{Min}$.[24,32] This corresponds to excitation at 248 nm and suggests that the $(n_O\pi^*)_X$ intersection is not relevant for any of the experiments related above. In 1MCyt, upper bounds of ~ 3100 and $\sim 5200 \, \text{cm}^{-1}$ for the barriers to access $(Eth)_X$ and $(OP)_X$ have been provided at the MS-CASPT2//CASSCF level.[35] Recently, the MS-CASPT2 barrier height for the decay through $(Eth)_X$ was estimated as $1600 \, \text{cm}^{-1}$.[36]

An early study on triplet formation in Cyt indicated the occurrence of competitive intersystem crossing (ISC) at a region of high spin-orbit coupling (SOC) along the decay path to the $(n_O\pi^*)_X$ state.[37] However, that study only gives a partial account of the possible mechanisms since the ethylenic and out-of-plane mechanisms were not considered at that time. Intersystem

crossing on a time-scale competitive with the radiationless decay was observed in a trajectory surface hopping (TSH) dynamics study carried out at the CASSCF level.[38] More recently, $S_1 \rightarrow T_1$ ISC has been suggested as the mechanism for formation of the triplet after excitation near the origin.[17]

In this context, our joint experimental and theoretical study combining R2PI and UV/UV holeburning spectroscopy of 1MCyt with high level ab initio calculations addresses several goals: (1) To interpret and explain the vibronic structure of the $S_0 \rightarrow S_1$ R2PI spectrum, which depends on the change between the S_0- and S_1-state structures and the excited-state vibrations that are activated by the optical excitation. In order to check the possible involvement of the methyl group rotation, we have also measured the isotopomer 1-(d_3)-methylcytosine [1-(d_3)-MCyt]. (2) To investigate the decay mechanism of 1-MCyt and 1-(d_3)-MCyt that leads to the break-off of the vibronic structure about 500 cm^{-1} above the 0_0^0 band of the $S_0 \rightarrow S_1$ spectrum, to assign a decay path with MS-CASPT2//CASSCF calculations, and to measure the internal conversion rates k_{IC} as a function of S_1 state excess vibrational energy E_{exc}. (3) To confirm the formation of a long-lived triplet state measured by R2PI at long delays,[9,10] to study the intersystem crossing (ISC) rate constants as a function of E_{exc}, and determine its mechanism of formation.

II.   COMPUTATIONAL AND EXPERIMENTAL METHODS

A.   Theoretical Methods

A uniform theoretical treatment of the ground- and excited-state potential energy surfaces of 1MCyt is difficult, and we have combined several theoretical approaches. The ground-state calculations have been carried out at the B3LYP, spin-component-scaled (SCS) resolution-of-identity (RI) Møller-Plesset (MP2) and SCS approximate second-order coupled-cluster (CC2) levels of theory with the TZVP, aug-cc-pVTZ and aug-cc-pVDZ basis sets, respectively. The excited-state calculations in the vicinity of the Franck-Condon (FC) region (vertical spectrum and excited-state minima) have been done at the time dependent (TD) CAM-B3LYP/6-311G* and SCS-CC2/aug-cc-pVDZ levels of theory. Finally, the CI optimization and the calculation of the reaction paths have been carried out with CASSCF/6-311G** because of the multi-referential character of the wave function in these regions. To provide a uniform global description, the final excited-state energies are obtained from MS-CASPT2 single-point calculations on the optimized structures using the ANO-L basis contracted to 4s3p2d for C, N and O and 3s2p1d for H. For the CASPT2 calculations we have used an imaginary level shift[39] of 0.1 a.u.

and the standard ionization potential - electron affinity correction[40] of 0.25 a.u.

The active space for the MS-CASPT2 /ANO-L calculations at the FC region is (14,10) (14 electrons in 10 orbitals) and incudes the 8 π orbitals and the two lone pairs on the oxygen and nitrogen atoms. The underlying wave function has been averaged over 8 states with equal weights, and all states are included in the MS-CASPT2 treatment. The active space of the CASSCF calculations of the excited-state decay paths and the corresponding MS-CASPT2 single-point calculations was specifically tailored for each path (see Supplementary Material for details). This procedure yields the CI structures with small MS-CASPT2 S_1/S_0 energy gaps of 887 cm^{-1} (0.11 eV) at $(Eth)_X$ and 2820 cm^{-1} (0.35 eV) at $(OP)_X$. To calculate the reaction paths we have optimized the transition structures (TS) on S_1, and the paths were obtained combining the intrinsic reaction coordinate[41] and initial relaxation direction[42] techniques. The calculated barriers also include vibrational zero-point energy (ZPE) corrections, based on CASSCF frequencies at $(^1\pi\pi^*)_{Min}$ (with $3N-6$ vibrational modes) and at the corresponding TS (including $3N-7$ modes). The CI were optimized using the recently developed double Newton-Raphson algorithm.[43] The calculations were performed using Turbomole 6.4,[44,45] a modified version of Gaussian09[46] and Molcas 7.8.[47,48]

B. Experimental Methods

1MCyt and 1-d_3-MCyt were synthesized as described in the literature.[49] The molecular-beam/ mass spectrometer experimental setup has been previously described.[50] Neon carrier gas at 1.8 bar backing pressure is passed through a 0.4 mm diam. pulsed nozzle containing 1MCyt or 1-d_3-MCyt heated to 220° C. Mass-selected two-color resonant two-photon ionization (2C-R2PI) spectra over the $31200 - 33000$ cm^{-1} range are measured by crossing the skimmed supersonic jet with unfocused UV excitation and ionization laser beams in the source of a linear time-of-flight mass spectrometer. Excitation is performed with the frequency-doubled output of a NarrowScan D-R dye laser ($0.4 - 0.6$ mJ/pulse), which is reduced to 0.3 mJ/pulse for the rotational contour measurements. The laser bandwidth in the UV is 0.053 cm^{-1} (1600 MHz) full-width at half-maximum (FWHM). The UV ionization pulses at 223 nm are generated by an Ekspla NT342B UV optical parametric oscillator (OPO) (1.5 mJ/pulse, 5 cm^{-1} bandwidth). Photoionization efficiency curves of 1MCyt are measured by fixing the excitation laser at the $0_0^0 + 64$ cm^{-1} band and scanning the ionization wavelength. A second frequency-doubled dye laser (~ 2 mJ/pulse) is employed for UV/UV holeburning or depletion experiments. The holeburning (or depletion) laser pulse precedes the detection laser pulse by 300 ns. In a UV/UV holeburning experiment, the burning laser is fixed at the desired vibronic transition and the de-

tection laser is scanned. The ion signal is measured at each wavelength on alternating laser shots with and without burn laser. Subtracting the unburned spectrum from the burned one yields the UV holeburning spectrum. For UV/UV depletion the detection laser is fixed at a specific vibronic transition, producing a constant ion signal. The UV depletion laser is scanned; when the depletion laser is in resonance with a vibronic transition of the same species that is being detected, the ion signal is reduced, giving a dip in the depletion spectrum.

Excited-state lifetimes and intersystem crossing (ISC) transients are measured by ns and ps excitation/delayed ionization, keeping the excitation and ionization wavelengths fixed. In the ns experiment, the time delay between the excitation and ionization lasers pulses is scanned by a computer-controlled digital delay unit (1.5 ns accuracy, 60 ps RMS jitter). The picosecond excitation/delayed ionization delay method has been described elsewhere.[51,52] Briefly, the 20 ps UV excitation pulse is generated by an Ekspla PG401 OPO/OPA system. The 20 ps ionization pulses at 266 nm are generated by quadrupling the ps Nd:YAG pump laser, and the 213 nm pulses are produced by mixing the 266 nm with the remaining 1064 nm. The transients and excited-state lifetimes τ are fitted with a program written in Interactive Data Language (IDL),[53] see ref. 17. The fit model includes an exponential decay for the optically excited S_1 state and an exponential increase for triplet state formed in the ISC process. The instrumental response function (IRF) is given by the convolution of the excitation and ionization laser pulses and is 7 ns FWHM for the ns experiment, as determined by fitting to the rise of the transient. The ps excitation/ionization IRF was measured to be 28 ps FWHM.[15,51,52]

III. RESULTS AND DISCUSSION

A. Resonant Two-Photon Ionization and UV/UV Holeburning Spectra

The vibrationally resolved two-color $S_0 \rightarrow S_1$ R2PI spectra of 1MCyt and 1-d_3-MCyt in the $31250 - 32800$ cm^{-1} range with ionization at 223 nm are shown in Figure 2. Both spectra exhibit five to six intense vibronic bands plus many weaker bands up to ~ 500 cm^{-1} above the lowest-energy bands at 31852 and 31925 cm^{-1}, respectively. The UV/UV holeburning spectra of 1MCyt and 1-d_3-MCyt with depletion at the band at +455 cm^{-1} and +381 cm^{-1}, respectively, reproduce the 2C-R2PI spectra in detail, see Figures S1 and S3 (Supplementary Material). The holeburning spectra prove that all the vibronic bands observed in Figure 2 originate from the same tautomer and S_0 ground state level.

The electronic origins lie at 31852 cm^{-1} (1MCyt) and 31925 cm^{-1} (1-d_3-MCyt) with intensities that are $10 - 20$ % of the strongest vibronic bands. The low Franck-Condon factors of
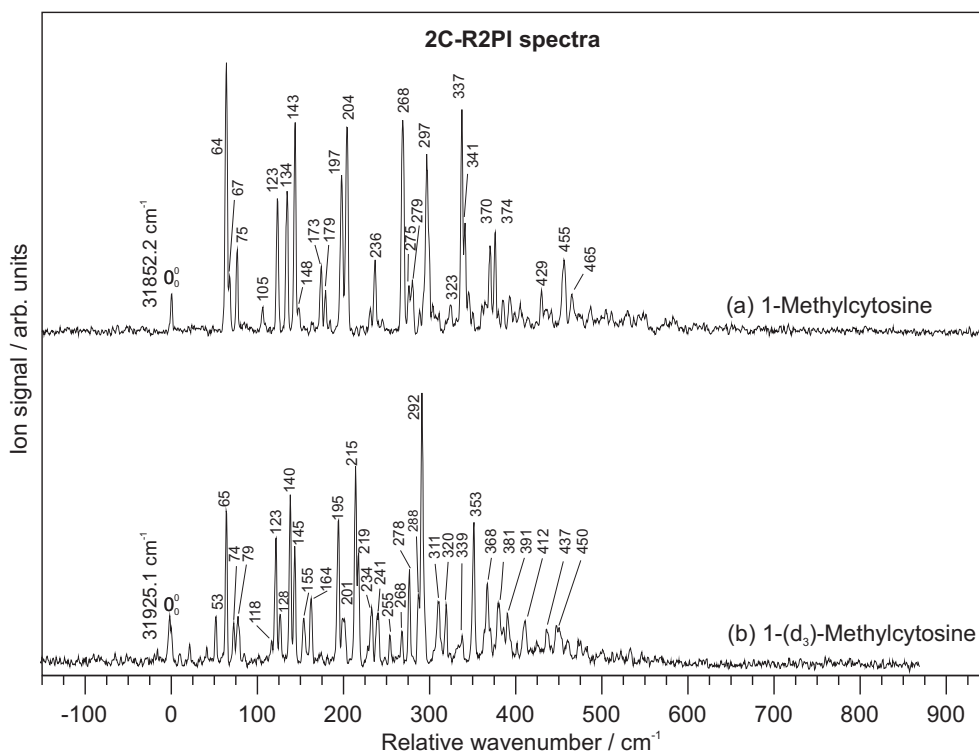
FIG. 2. Two-color resonant two-photon ionization spectra of supersonically cooled (a) 1MCyt and (b) 1-d_3-MCyt (ionization at 223 nm). Frequency scale relative to the $S_0 \rightarrow S_1$ electronic origins at 31852 cm^{-1} (1MCyt) and 31925 cm^{-1} (1-d_3-MCyt).

these 0_0^0 bands signal a marked geometry change between the S_0 and S_1 excited states. De Vries *et al.* assigned the intense band at $0_0^0 + 64$ cm^{-1}(at 31908 cm^{-1}) as the $S_0 \rightarrow S_1$ 0_0^0 band and attributed the origins assigned here to hot bands; they mentioned UV/UV depletion spectra but did not show them in their paper.[9,10] The present UV/UV holeburning spectra call for revision of their assignment.

We also recorded the 2C-R2PI spectra of 1MCyt and 1-d_3-MCyt with the ionization laser tuned to 215 nm, where triplet signal is detected (see below) and with the ionization delayed by 30 ns relative to the excitation laser, so that only triplet molecules are ionized. The delayed R2PI spectra are identical to the prompt two-color R2PI spectra and break off at ~ 500 cm^{-1} as well, suggesting that a barrier to internal conversion (IC) is exceeded at this energy level (see Figures S4 and S5 in the Supplementary Material).

B. Vertical and Adiabatic Excitations

Tautomers of 1-Methylcytosine: 1MCyt can exist in the different tautomer/rotamer forms shown in Figure 1. The relative ground-state energies are given in Table I. All computational methods predict the amino-keto tautomer **1** as the most stable by ≥ 1.1 kcal/mol, and we expect it to be the dominant species in the supersonic jet. The imino-keto-trans **3a** and imino-keto-cis **3b**

8

tautomers are $1.1 - 3.0$ and $1.8 - 4.7$ kcal/mol higher, respectively. The imino-enol tautomers and rotamers are even higher, by 20 kcal/mol or more. To assess the putative contributions of the tautomers **3a** and **3b** to the spectra, we calculated their lowest $^1\pi\pi^*$ adiabatic transition energies. At the TD-B3LYP level, these are $2050 - 2700$ cm^{-1} higher than that of the amino-keto form **1**. We therefore only consider tautomer **1** from now on.

Excitation Spectrum: Table II shows the SCS-CC2/aug-cc-pVDZ and MS-CASPT2(14,10)/ANO-L calculated adiabatic and vertical transition energies for the amino-keto **1** tautomer. Both the SCS-CC2 and the MS-CASPT2 methods predict that the S_1 state is predominantly of $^1\pi\pi^*$ character. At the SCS-CC2 level, S_1 also has 17% $n\pi^*$ character. The adiabatic $S_0 \to S_1$ transition energies are 31899 cm^{-1} and 31429 cm^{-1} at the SCS-CC2 and the MS-CASPT2 levels, respectively, in very good agreement with the experimentally observed 0_0^0 band at 31852 cm^{-1}, see Figure 2. The calculated vertical excitations are in line with previous calculations.[14,54] The SCS-CC2 and MS-CASPT2 methods predict the lowest vertical $^1\pi\pi^*$ transition at 37049 cm^{-1} and 37449 cm^{-1}, respectively, with oscillator strengths $f_{el} \sim 0.1$. This is in good agreement with the experimental value of 37500 cm^{-1} for cytosine obtained from electron energy loss spectroscopic measurements.[55] The lowest $^1n\pi^*$ state, S_2, appears at approximately 42500 cm^{-1} with both methods. Finally, S_3 and S_4 at the MS-CASPT2 level appear as two close-lying transitions around 46000 cm^{-1} with mixed $^1\pi\pi^*$ and $^1n\pi^*$ character.

TABLE I. Calculated ground-state energies (in kcal/mol) of the seven tautomers/rotamers of 1MCyt at various levels of theory, relative to the amino-keto **1** tautomer.

method/basis	1	3a	3b	1.1	1.2	1.3	1.4
B3LYP/TZVP	0.00	2.14	3.97	30.49	20.44	23.96	34.98
SCS-CC2/aug-cc-pVDZ	0.00	1.61	3.28				
SCS-MP2/aug-cc-pVTZ	0.00	1.12	2.83				
G3MP2B3/—[a]	0.00	1.76	1.76				
MS-CASPT2/6-31G*[b]	0.00	2.31	3.92				
MP2/6-311G**[c]	0.00	1.78	3.54				
B3LYP/6-31+G*[d]	0.00	2.9	4.6		21.4	24.8	
B3-MP2/6-311++G(df,2p)[e]	0.00	2.94	4.73				
B3LYP/6-31++G**[f]	0.00	2.53	4.34				
MP2/aug-cc-pVDZ[f]	0.00	2.34	4.09				
CCSD(T)/aug-cc-pVDZ[fg]	0.00	1.42	3.09				

[a] Ref. 14.
[b] Ref. 35 (CASPT2(16,12)/ANO-S//CASSCF(14,10)/6-31G*).
[c] Ref. 56.
[d] Ref. 57.
[e] Ref. 58 (Single-point energies with B3LYP/6-31+G(d,p) zero-point energy corrections).
[f] Ref. 59.
[g] Single-point energies on the MP2/aug-cc-pVDZ structure.

TABLE II. SCS-CC2 and MS-CASPT2 calculated adiabatic and vertical transition energies (in cm^{-1}) and oscillator strengths f_{el} for the amino-keto **1** tautomer of 1MCyt.

| State | SCS-CC2/aug-cc-pVDZ | | MS-CASPT2/ANO-L[b] | | Experimental |
	vertical (f_{el}[a])	adiab.	vertical (f_{el}[a])	adiab.	adiab.
S_1 ($^1\pi\pi^*$)	37049 (0.0876)	31899	37449 (0.1035)	31429[c]	31852 ± 1
S_2 ($^1n\pi^*$)[d]	42537 (0.0066)	36948	42411 (0.0028)		
S_3[e]	44169 (0.0155)		45870 (0.0091)		
S_4[e]	45578 (0.0599)		46098 (0.0770)		
T_1 ($^3\pi\pi^*$)	30668	28563	31560	27862	25600 ± 500
T_2 ($^3\pi\pi^*$)	38121		39167		
T_3 ($^3n\pi^*$)	41231		41299	33529[f]	
Ion ground state (D_0)	77043	71904			68350 ± 200

[a] Vertical excitation from S_0 equilibrium geometry, length representation.
[b] At CAM-B3LYP optimized geometries, details see text.
[c] Includes ZPE correction of -1013 cm^{-1} calculated at the CAM-B3LYP/6-311G** level of theory.
[d] Excitation mainly from the oxygen lone pair.
[e] States with mixed $^1\pi\pi^*/^1n\pi^*$ character.
[f] State becomes T_2 upon optimization, excitation mainly from the nitrogen lone pair.

Excited-State Structures: The structure of the S_1 minimum, $(\pi\pi^*)_{Min}$, depends on the level of theory used for the optimization. A quasi-planar minimum, pyramidalized at C_6, is obtained with the CASSCF(10,8)/6-311G**, MS-CASPT2(8,7)/DZP,[36] CC2/aug-cc-pVDZ and TD-B3LYP/TZVP methods, whereas a ring-puckered structure is obtained at the CASSCF(12,11)/6-311G**, SCS-CC2/aug-cc-pVDZ and TD-CAM-B3LYP/6-311G** levels. The different S_1 minima have also different bond lengths. For instance, the C_2-O_7 bond length varies from 1.255 Å with TD-CAM-B3LYP to 1.320 Å with CASSCF(12,11) and 1.354 Å with SCS-CC2 (see Supplementary Material for details). Good agreement with the experimental adiabatic transition of 31852 cm^{-1} is obtained at the TD-B3LYP, MS-CASPT2(8,7) and SCS-CC2 levels of theory. However, the three methods give substantially different structures, and the main question is whether the 0_0^0 transition leads to a quasi-planar structure, as suggested by B3LYP and MS-CASPT2(8,7), or a ring-puckered structure as suggested by SCS-CC2 and TD-CAM-B3LYP. To solve this question, the energies of all structures were recalculated at the MS-CASPT2(14,10)/ANO-L level. The lowest S_1 energy at this level is obtained for the TD-CAM-B3LYP and CASSCF(12,11) optimized structures, for which the ring is puckered. The relative potential energies without ZPE correction are 32442 and 32771 cm^{-1}, respectively. Thus, the SCS-CC2 and the MS-CASPT2(14,10) calculations on the structures optimized with different methods agree that $(\pi\pi^*)_{Min}$ has a ring-puckered structure. This agrees with the small intensity of the experimental 0_0^0 transition, see above, and with the large Franck-Condon factors in out-of-plane vibrations, see below. The overlay of the S_0 and S_1 minima obtained at the SCS-CC2 level (Figure 3) shows that, together with the ring puckering, the methyl group
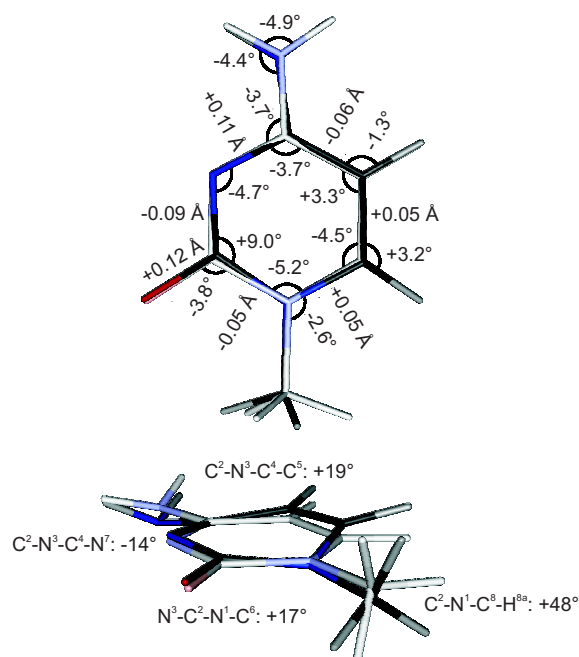
FIG. 3. SCS-CC2/aug-cc-pVDZ calculated geometry changes of 1MCyt upon $^1\pi\pi^*$ excitation; the excited state is in darker color. Only bond length changes ≥ 0.05 Å and angle changes $\geq 1°$ are indicated.

undergoes a rotation upon $S_0 \rightarrow S_1$ excitation of $48°$ (SCS-CC2) and $60°$ (TD-B3LYP), see also Section III F.

The large variations of the minimum structures predicted by the different theoretical methods point to the importance of vibronic (or pseudo-Jahn-Teller) interactions between the close-lying $^1\pi\pi^*$ and $^1n\pi^*$ states, which leads to breaking of the ring planarity and puckering of the ring.[60,61] The $^1\pi\pi^* \leftrightarrow {}^1n\pi^*$ vibronic interaction is the cause for the differences found between similar ab initio methods. Thus, SCS-CC2 and CASSCF(12,11) predict ring-puckered structures, whereas unscaled CC2 and CASSCF with a smaller (8,7) active space give a quasi-planar structure. In the coupled cluster case, SCS-CC2 is more suitable for cases with high electronic correlation such as the present one. In the CASSCF case the (12,11) active space was specially tailored to account for the vibronic interaction since it includes the oxygen lone pair responsible for the $^1n\pi^*$ excitation and a 3p orbital on the oxygen to account for radial correlation. For the same reason, the MS-CASPT2 optimization with the reduced (8,7) active space,[36] which lacks the oxygen lone pair responsible for the interaction gives a quasi-planar structure whose MS-CASPT2(14,10) energy is approximately 800 cm^{-1} higher than the TD-CAM-B3LYP optimized structure.

C. Nanosecond Excitation/ Delayed Ionization Measurements

Figure 4(a) shows the nanosecond excitation/delayed ionization transients for 1MCyt and 1-d_3-MCyt, measured at the 0_0^0+64 cm^{-1} and 0_0^0+65 cm^{-1} bands with ionization at 223 nm. The initial peak ("prompt" ionization signal) corresponds to ionization of the optically excited $S_1(^1\pi\pi^*)$ state. The nearly flat "tail" extending to longer delay time corresponds to the ionization of a long-lived state, which is shown to be the T_1 triplet state in section III D. The ns excitation/ionization transient for 1-d_3-MCyt is similar to 1-MCyt, the long-lived component being 11% higher.

Figure 4(b) shows the dependence of the ns transient for 1MCyt on the ionization wavelength. For ionization wavelengths > 240 nm only prompt ionization signal is observed; with decreasing ionization wavelength (increasing ionization energy) the delayed signal increases relative to the prompt signal, reaching 50 % of the prompt signal at 215 nm.
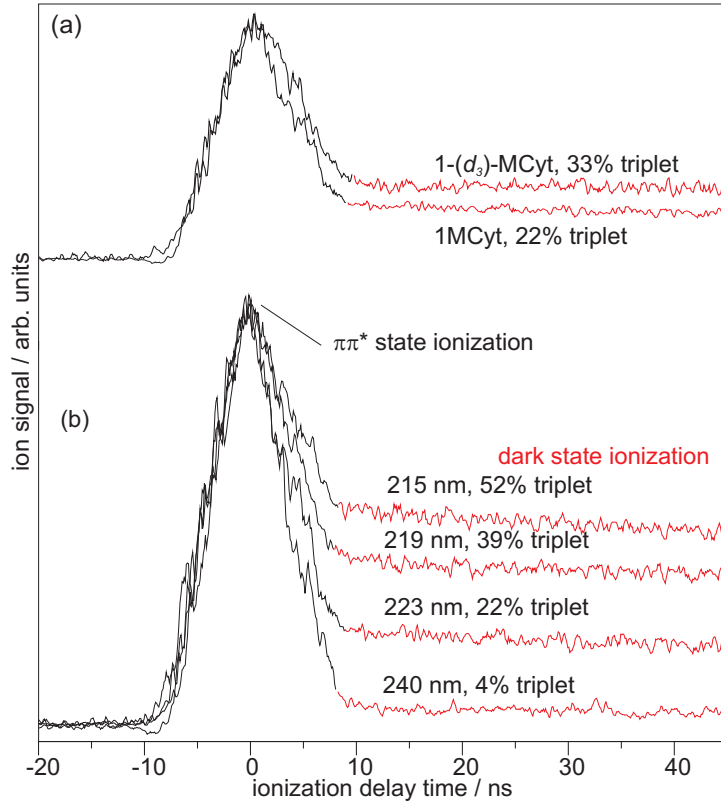

FIG. 4. (a) Ionization delay curves for 1MCyt and 1-d_3-MCyt excited at the 0_0^0+64 cm^{-1} band (31916 cm^{-1}) and 0_0^0+65 cm^{-1} band (31992 cm^{-1}), with ionization at 223 nm. (b) Nanosecond ionization delay curves of 1-MCyt for the series of ionization wavelengths $215 - 240$ nm.

The percentages of triplet ion signal are noted above the delayed transient in Figure 4(b); they are related to the ionization cross-section σ_{ion}^+ of the triplet state relative to the S_1 state, as will be discussed in section III D. In section III E we show that the S_1 state lifetime at 0_0^0+64 cm^{-1} is ~ 10 times shorter than the 5 ns pulse lengths of the excitation and ionization lasers. In

contrast, the T_1 lifetime is ~ 200 ns and thus much longer than the laser pulse length. Hence, the efficiency with which a given S_1 vibronic level is ionized depends on its lifetime, relative to the 5 ns laser pulse length, so the detection efficiencies decrease for the higher S_1 vibronic levels with shorter lifetimes (see section III E). The relative singlet and triplet ion signal in the ns pump/ionization transients depend on the lifetime of the S_1 level and on the ratio of the ionization cross sections $\sigma_{ion}^+(S_1)/\sigma_{ion}^+(T_1)$, both must be taken into account when modeling the ns excitation/ionization transients, as previously discussed for cytosine.[17] We discuss the fitting of the ISC rates in combination with the ps excitation/ionization transients in Section III E.

D. Photoionization Efficiency Curves and Thresholds

Figure 5 shows two photoionization efficiency (PIE) curves of 1-methylcytosine as a function of ionization laser energy, both measured when exciting at the 0_0^0+64 cm^{-1} band (31852 cm^{-1}). The black curve is measured at the prompt ionization peak, corresponding to ionization of the S_1 state. The red curve is measured with the ionization pulse delayed by 50 ns, corresponding to ionization of the long-lived state. The relative heights of the prompt and delayed PIE curves are scaled according to the ratio of the prompt and 50 ns delayed signals in Figure 4. The S_1 state ionization threshold is observed at 36000 ± 200 cm^{-1}; the ion signal rises slowly above the background, does not exhibit a step-like onset and thus is an upper limit to the adiabatic ionization energy. The sum of the excitation and the ionization threshold corresponds to a ionization energy $IE = 67850 \pm 200$ cm^{-1} or 8.41 ± 0.03 eV. Compared to amino-keto cytosine which has an adiabatic ionization energy IE of 8.73 ± 0.02 eV,[16] the methyl substitution at N$_1$ lowers the ionization energy by at least 0.32 eV.

The onset of the delayed-ionization PIE curve in Figure 5 at ~ 41200 cm^{-1} is 5200 cm^{-1} above the S_1 threshold, with a slower initial rise above the background. If we assume that the 5200 cm^{-1} correspond to the adiabatic energy difference between S_1 and the lower-lying long-lived state, this energy difference is randomized over the 42 vibrational modes of 1MCyt after the 50 ns delay time. We thus interpret the sluggish onset of the delayed-ionization PIE curve between $41000 - 42250$ cm^{-1} as photoionization from vibrationally hot triplet states that contribute ion signal below the "cold" ionization threshold. Similar to the procedure in ref. 16, we estimate the cold ionization threshold by back-extrapolation of the linear rise of the PIE curve to the zero-ion-signal background, giving 42250 ± 500 cm^{-1}. Comparing this estimate of the ionization energy of the long-lived state to the IE measured via the S_1 state implies that the long-lived state lies about 25600 ± 500 cm^{-1} (3.17 ± 0.06 eV) above the S_0 state.

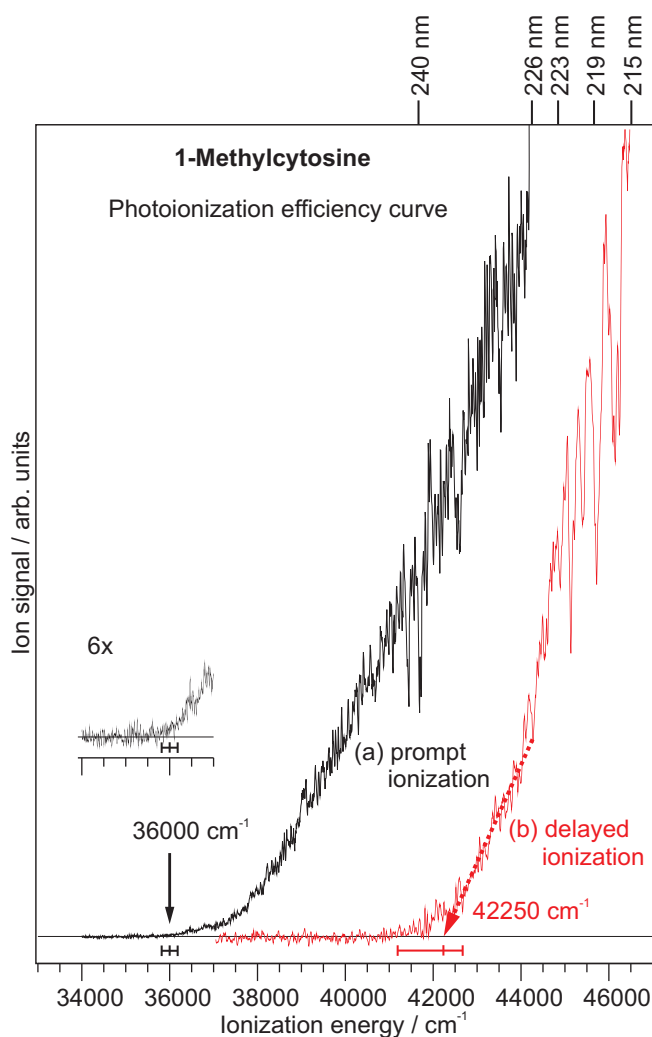Table II shows that of all the calculated excited states of 1MCyt, only $T_1(^3\pi\pi^*)$ has ap-

FIG. 5. Photoionization efficiency curves for (a) prompt (0 ns delay) and (b) 50 ns delayed ionization of 1MCyt, when exciting the $0_0^0 + 64$ cm^{-1} band. Uncertainties indicated with horizontal bars.

proximately this energy, hence we consider the assignment of the long-lived dark state as established. Also, the T_1 state should have a long lifetime, as is observed experimentally. The SCS-CC2 (28563 cm^{-1}) and the MS-CASPT2 (27862 cm^{-1}) $T_1(^3\pi\pi^*)$ energies are about 3000 and 2200 cm^{-1} higher, respectively, than the experimental value. At the MS-CASPT2 level of theory, the adiabatic energy of T_2 which has $(n\pi^*)$ character, is 33529 cm^{-1} (see Table II).

Comparison of the $IE = 67850 \pm 200$ cm^{-1} with the vertical and adiabatic calculated ionization energies in Table III shows that (1) the SCS-CC2 ionization energies are consistently higher than those calculated with all other methods. (2) The experimental IE is about 1000 cm^{-1} higher than the B3LYP calculated ionization energies and (3) about 1000 cm^{-1} lower than the vertical IEs from photoelectron spectra, P3 electron propagator/6-311G** and OVGF-MP2/6-311G(d,p) calculations.[56,62,63] Since a large geometry change is expected for the $S_1 \rightarrow D_0$ transition, the Franck-Condon factor of the adiabatic transition in ionization is expected to be very small.

14

TABLE III. Calculated and experimental ionization energies of 1MCyt (in cm^{-1}).

	Vertical			Adiabatic		
Method	$S_0 \to D_0$	$S_1 \to D_0$	$T_1 \to D_0$	$S_0 \to D_0$	$S_1 \to D_0$	$T_1 \to D_0$
PIE curve (this work)				67850 ± 200	36000 ± 200	42250 ± 500
B3LYP/TZVP	67321	39172	46217 (T_1)	66338	34312	40772 (T_1)
SCS-CC2/aug-cc-pVDZ	77043	44839	56248 (T_1)	71904	40005	43341 (T_1)
B3LYP/6-31+G(d,p) [a]	67920			66640		
P3 propagator/6-311G** [b]	68800					
OVGF-MP2/6-311G(d,p) [c]	68800					
Photoelectr. spectr.(exp.) [d]	69760					

[a] Ref. 14
[b] Ref. 56
[c] Ref. 62
[d] Ref. 63

E.   Picosecond Excitation/ Delayed Ionization Measurements

Figure 6(a) shows the ps two-color resonant two-photon ionization overview spectrum of 1MCyt with ionization at 213 nm. Note the different band intensities and overall shape, compared to the ns laser R2PI spectrum in Figure 2. While the 0_0^0 band at 31852 cm^{-1} is clearly observed in the ns spectrum, it is hardly detectable in the ps R2PI spectrum. The following three bands in the ns R2PI spectrum are among the most intense transitions, but are rather small in the ps spectrum. The band at $+460$ cm^{-1} just before the spectrum breaks off is weak in the ns spectrum, but is the most intense band in the ps R2PI spectrum. We show below that the reason for the large difference between the ns and ps R2PI spectra results from the fact that the S_1 state lifetimes decrease by a factor of $50 - 70$ over the vibrational excess energy range $E_{exc} = 0 - 500$ cm^{-1} in the S_1 state.

The S_1 ($^1\pi\pi^*$) state kinetics is modeled as

$$\frac{d[S_1]}{dt} = -(k_{rad}^{S_1} + k_{IC}^{S_1} + k_{ISC}^{S_1}) \cdot [S_1] \tag{1}$$

where k_{rad} is the $S_1 \to S_0$ radiative decay rate. The SCS-CC2 calculated oscillator strength of 1MCyt is $f_{el} = 0.0876$, giving $\tau_{rad} \approx 12$ ns or $k_{rad} = 8.3 \cdot 10^7$ s^{-1}. The S_1 state decays nonradiatively to S_0 by internal conversion (IC) with the rate constant $k_{IC}^{S_1}$. Since the $^1n\pi^*$ state is calculated to lie above the $^1\pi\pi^*$ state, see Section III B, relaxation to the $^1n\pi^*$ state is not included in the kinetic model. The third term in eqn.(1) expresses the formation of the T_1 from S_1 with the intersystem crossing (ISC) rate constant $k_{ISC}^{S_1}$, see Sections III C and III D. We assume that T_1 relaxes to S_0 by $T_1 \rightsquigarrow S_0$ ISC as well as by phosphorescence, these two
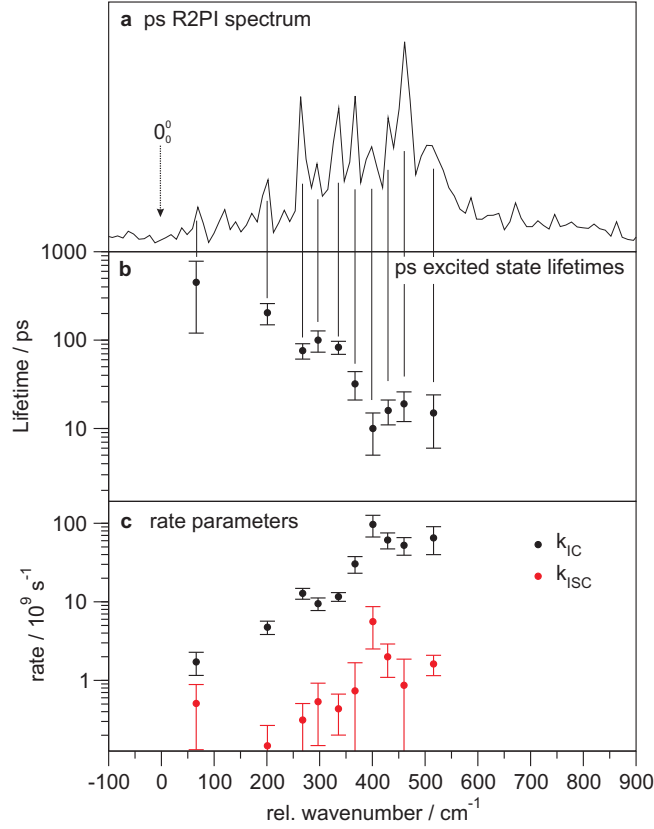
FIG. 6. (a) Picosecond R2PI spectrum of 1MCyt; (b) excited-state lifetime τ, measured at the vibronic bands indicated. (c) Experimental internal conversion and intersystem crossing rate constants, see also Table IV.

pathways are combined into a single rate constant k_T:

$$\frac{d[T_1]}{dt} = k_{ISC}^{S_1} \cdot [S_1] - k_T \cdot [T_1] \tag{2}$$

The ns excitation/ionization transients show that the T_1 decay is on the ~ 200 ns timescale, so k_T is small compared to the other rates and is set to zero for the fits. Using the calculated k_{rad}, the rate constants $k_{ISC}^{S_1}$ and $k_{IC}^{S_1}$ are least-squares fitted to the ten measured transients. The experimental ps pump/ionization transients are shown in Figure 7. The fitted signal contribution from $S_1(^1\pi\pi^*)$ is plotted in blue, that from T_1 in yellow, and the sum of both populations in red. As both $k_{ISC}^{S_1}$ and $k_{IC}^{S_1}$ are longer than the inverse of the 28 ps time resolution of the ps pump-ionization experiment (section II.B) the ps transients do not need to be corrected for the relative lifetime effects.

Figure 6(b) shows the excited-state lifetimes $\tau = 1/(k_{rad} + k_{IC}^{S_1} + k_{ISC}^{S_1})$ determined from the ps pump/ionization transients measurements at ten vibronic bands, as indicated by the vertical lines. The experimental transients are plotted in black in Figure 7. The lifetimes and 1σ error bars in Figure 6(c) are determined by fitting four to eight transients at the same wavelength. The
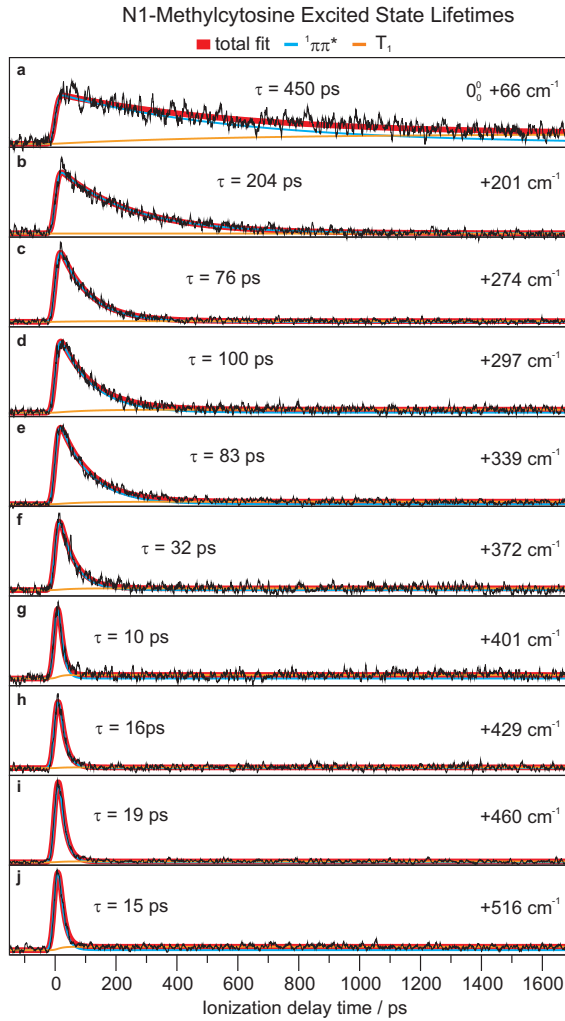
16

FIG. 7. Picosecond excitation/delayed ionization transients of 1MCyt, with ionization at 213 nm. Black: experimental, blue: S_1 decay, yellow: T_1 increase, red: total fit. The indicated wavenumbers (relative to the 0_0^0 band) are center values of the output of the UV-OPO/OPA. Because of the $\sim 4\ \mathrm{cm}^{-1}$ step-size of the UV-OPO, these do always coincide exactly with the band maxima in the ns laser R2PI spectrum in Figure 2a.

$S_1\ 0_0^0$ lifetime could not be measured due to the weakness of this band, see Figure 6(a). The lowest-energy vibronic band in the ps R2PI spectrum at $0_0^0 + 66\ \mathrm{cm}^{-1}$ is also weak. We have recently reported the lifetime as $\tau = 600 \pm 290$ ps,[15] but by measuring 8 separate transients on different days we have decreased the uncertainty by nearly a factor of two, the revised value is $\tau = 450 \pm 160$ ps. At $+200\ \mathrm{cm}^{-1}$, the lifetime decreases to 230 ps, and continues to decrease up to the shortest measurable lifetime $\tau = 15$ ps at $400\ \mathrm{cm}^{-1}$ above the 0_0^0 band. Table IV summarizes the fitted internal conversion and intersystem crossing rate constants, as well as the corresponding lifetimes $\tau = 1/(k_{rad} + k_{IC}^{S_1} + k_{ISC}^{S_1})$.

Contrary to the ns transients shown in Figure 4, the ps transients exhibit only a small signal increase from the growing-in of the T_1 state population. Figure 6(c) and Table IV show that in the nonradiative relaxation of 1MCyt, ISC is only significant for the $0_0^0 + 64\ \mathrm{cm}^{-1}$ level, at

TABLE IV. Intersystem crossing (ISC) and internal conversion (IC) rate constants, from fits to the ps excitation/ionization transients in Figure 7.

Band/ cm^{-1} [a]	$k_{ISC}^{S_1}$/ 10^9 s^{-1} [b]	$k_{IC}^{S_1}$/ 10^9 s^{-1} [b]	Lifetime τ/ ps [b]
$0_0^0 + 66$	0.5 ± 0.4	1.7 ± 0.6	450 ± 160
$+201$	0.2 ± 0.1	4.8 ± 0.9	204 ± 55
$+274$	0.3 ± 0.2	12.8 ± 2.0	76 ± 15
$+297$	0.5 ± 0.4	9.5 ± 1.7	100 ± 27
$+339$	0.4 ± 0.2	12 ± 2.0	83 ± 14
$+372$	0.7 ± 0.9	30 ± 7.0	32 ± 12
$+401$	5.6 ± 3.1	100 ± 30	10 ± 5
$+429$	2.0 ± 0.9	61 ± 14	16 ± 5
$+460$	0.9 ± 1.0	52 ± 13	19 ± 7
$+516$	1.6 ± 0.5	65 ± 25	15 ± 9

[a] Laser excitation frequency relative to the 0_0^0 band at 31852 cm^{-1}.
[b] Measurement 1σ uncertainty; standard deviation from fitting four to eight separate transients.

which $k_{IC}^{S_1}$ is relatively small and k_{ISC} is only three times lower than k_{IC}. For the following vibronic levels, the rise in k_{IC} by up to $30 - 40$x overwhelms the slower rise in k_{ISC}. The
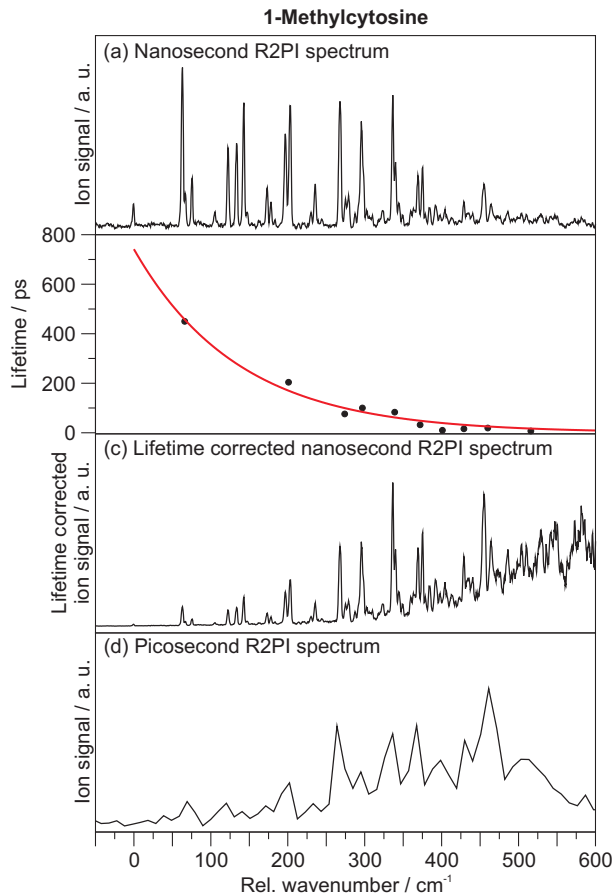

FIG. 8. (a) Nanosecond R2PI spectrum of 1MCyt, ionization at 226 nm. (b) Excited-state lifetimes, red line is an interpolation of lifetimes τ at the corresponding bands in Figure 6(b). (c) Lifetime-corrected nanosecond R2PI spectrum. (d) Picosecond R2PI spectrum of 1MCyt, see Figure 6(a).

knowledge of the single vibronic-level lifetimes now allows to explain the marked difference

between the ps and ns R2PI spectra. Figure 8(a) shows the ns R2PI spectrum, see also Fig. 2(a). Figure 8(b) plots an exponential model function that was nonlinear least-squares fitted to the vibronic band lifetimes of Figure 6 and Table IV. Since the probability of ionizing the S_1 state vibronic levels with a 5 ns ionization pulse decreases with the decreasing lifetime of the state, we can remove the ionization bias of the ns R2PI spectrum by dividing it by the red lifetime curve in Figure 8(b). The resulting lifetime-corrected ns R2PI spectrum is shown in Figure 8(c) and compared to the experimental ps R2PI spectrum in Figure 8(d). Apart from the ~ 20 times lower resolution of the ps spectrum, one observes a good agreement of the two spectra up to about $+550$ cm^{-1}. The two advantages of the lifetime-corrected ns R2PI spectrum are that (1) this procedure gives correct vibronic band intensities (Franck-Condon factors) which can be compared to those derived from ab initio calculations, and (2) the spectral information is obtained at the ~ 0.5 cm^{-1} resolution of the ns laser and not at the much lower resolution of the ps laser.

F. Methyl Group Internal Rotation

As pointed out in Section III B, the S_1 minimum of 1MCyt, $(\pi\pi^*)_{Min}$, shows strong ring-puckering and the methyl group is rotated by $48° - 60°$ relative to the S_0 minimum at the CASSCF(12,11)/6-311G** , TD-CAM-B3lYP/6-311G** and SCS-CC2/aug-cc-pVDZ levels of theory. This suggests large displacements along at least one out-of-plane vibration and the methyl torsional mode. To assign the spectra of 1MCyt and 1-d_3-MCyt, we performed a PGO-PHER vibronic simulation , see section G. However, the methyl-rotor transitions are highly anharmonic and were treated using a one-dimensional (1D) internal-rotation Hamiltonian in the S_0 and S_1 ($^1\pi\pi^*$) states.

We define the methyl torsional angle ϕ as the dihedral angle H$_a$-C$_2$-N$_1$-C$_8$, see Figure 1. Starting from the respective minimum-energy structures, the 1D torsional potentials were calculated by incrementing ϕ in steps of $10°$, optimizing all other structure parameters at each step. In the SCS-CC2 S_1 state, the N^3-C^2-N^1-C^6 and C^6-C^5-C^4-N^3 ring dihedrals had to be fixed to obtain a potential describing a pure torsional motion. This suggests a coupling of the methyl rotation to one or more out-of-plane modes, see below. The methyl rotor potentials are well described by the function $V(\phi) = V_3 \cdot (1 - cos(3\phi + \varphi))/2$, where φ is the phase shift of the S_1 relative to the S_0 potential. $V''(\phi)$ and $V'(\phi)$ were fitted to the calculated S_0 and S_1 energies; they are shown in Figure S6 in the Supplementary Material. The reduced internal-rotation constants F_{red} were calculated according to the literature.[64] The torsional barriers V_3, reduced internal-rotation constants F_{red} and phase shifts φ are summarized in Table V at various levels

of theory.

TABLE V. Calculated methyl rotor parameters of 1MCyt and 1-d_3-MCyt. All values in cm^{-1} except φ.

Parameter	B3LYP	SCS-CC2	MS-CASPT2(10,8) [a]
	TZVP	aug-cc-pVDZ	ANO-L
F''_{red} (h_3) / F''_{red} (d_3)	5.42 / 2.77	5.29 / 2.71	
F'_{red} (h_3) / F'_{red} (d_3)	5.40 / 2.77	5.28 / 2.70	
V''_3	188	361	340
V'_3	606	591 / 630 [b]	500
φ (degrees)	60	48 / -49 [b]	61

[a] Single point energies on CASSCF(10,8)/6-311G** optimized geometries.

[b] Values for the *up-down* and *up-up* ring-puckering conformers, respectively. See Figure 9 (a) and (b). To obtain a potential of a pure methyl torsional motion, the N^3-C^2-N^1-C^6 and C^6-C^5-C^4-N^3 dihedrals (butterfly angle) had to be fixed, all other parameters were optimized.

The torsional eigenfunctions, eigenvalues and Franck-Condon factors were obtained by numerically solving the 1D torsional Hamiltonian with a home-written IDL[53] program based on the discrete variable representation, using the libraries of Dimeo.[65] To calculate the contribution of the methyl rotor bands to the spectrum, a ground state barrier of 200 cm^{-1} and the SCS-CC2 calculated internal-rotation constants F''_{red} and F'_{red} for 1MCyt and 1-d_3-MCyt, respectively, were used as an input and the excited state barriers were varied between 80 and 610 cm^{-1}. However, we could not find a barrier height that allows a satisfactory assignment of the methyl internal-rotor bands for both molecules. This suggests that the methyl torsion cannot be treated one-dimensionally, but that the methyl rotation is coupled to other out-of-plane modes, as predicted by the SCS-CC2 method. This provides indirect support for our assignment of the non-planar structure of $(\pi\pi^*)_{Min}$.

To understand the methyl rotor/out-of-plane coupling, a two-dimensional (2D) S_1 state potential was calculated at the SCS-CC2/aug-cc-pVDZ level. We define the butterfly coordinate as the two dihedrals N_3-C_2-N_1-C_6 and C_6-C_5-C_4-N_3 (both set to the same value), see Figure 1. The 2D-potential was calculated on a 5 degree grid along the butterfly coordinate and on a 10 degree grid along the methyl torsional coordinate. At each point the methyl torsional and butterfly coordinates were kept fixed (three dihedrals in total), all other parameters being optimized.

Figure 9(c) shows the 2D-potential, which exhibits an asymmetric double-minimum shape along the butterfly coordinate with a low barrier of ~ 400 cm^{-1}. Figure 9(a,b) shows the two ring-puckered minima, which are separated by ~ 80 cm^{-1}. They have different equilibrium methyl torsion angles, therefore interconversion between them involves motion along both coordinates. The two minima also have slightly different V_3 barriers, as listed in Table V. To elucidate the contribution of these two vibrations to the spectrum, we would need to solve the two-dimensional problem. Kleiner and Hougen have proposed an approach for solving 2D-

coupled motions in systems with a methyl rotor and a double-minimum oscillatory motion such as ring inversion.[66] Whereas their approach is optimal for eigenvalues far below the barrier,[66] we need eigenvalues also above the butterfly barrier of ~ 400 cm^{-1}. The problem is addition-

(c) two-dimensional S$_1$ state potential

(a) up-down minimum

butterfly angle = 15°
relative energy = 0 cm^{-1}

(b) up-up minimum

butterfly angle = -15°
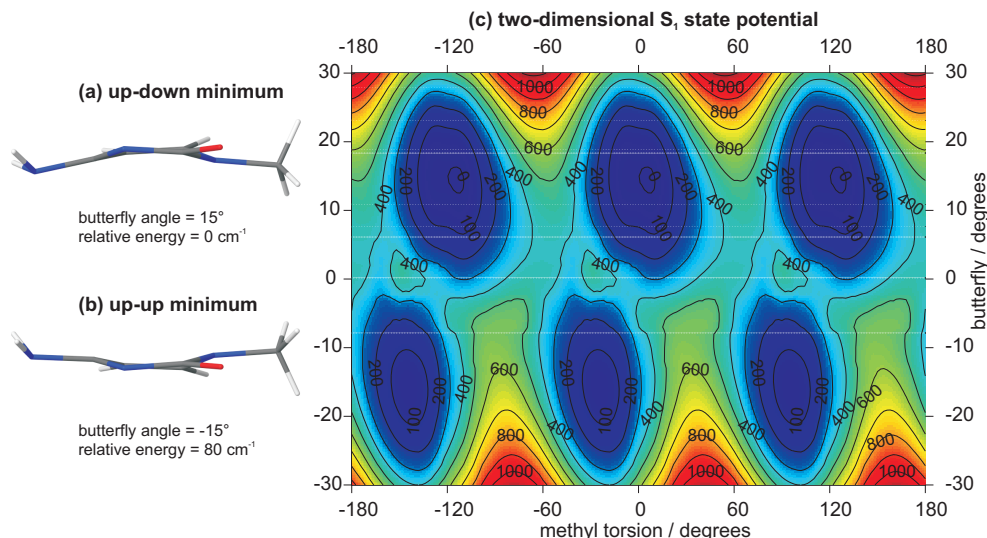relative energy = 80 cm^{-1}

FIG. 9. (a) The *up-down* and (b) *up-up* minimum structures of 1-methylcytosine. (c) SCS-CC2/aug-cc-pVDZ calculated S_1 state two-dimensional potential energy surface along the methyl torsional (x) and butterfly vibrational (y) coordinates, contours are spaced by 100 cm^{-1}. The x axis is given relative to the global minimum shown in (a). The y axis represents the value of the N^3-C^2-N^1-C^6 and C^6-C^5-C^4-N^3 angles.

ally complicated by the additional involvement of the NH$_2$ inversion mode, because besides the up-down and up-up minima in Figure 9 there are also the down-up and down-down minima.

G.   Vibronic Assignments

As pointed out in Section III B, the S_1 minimum of 1MCyt, $(\pi\pi^*)_{Min}$, shows strong ring-puckering with the methyl group rotated relative to the S_0 minimum at the CASSCF(12,11)/6-311G**, TD-CAM-B3lYP/6-311G** and SCS-CC2/aug-cc-pVDZ levels of theory. These large displacements suggest that long progressions should be observed involving at least one out-of-plane mode and the methyl torsion. The PGOPHER simulated vibronic band spectrum of 1MCyt using the SCS-CC2/aug-cc-pVDZ optimized S_0 and S_1 state equilibrium structures and harmonic wavenumbers is shown in Figure 10. To achieve better agreement with the experimental spectrum, the calculated wavenumber of the butterfly (ν_1') mode was decreased from 81.3 cm^{-1} to 66.5 cm^{-1} and that of ν_4' from 190.5 cm^{-1} to 173.3 cm^{-1}; the out-of-plane ν_2', ν_5', ν_7' and ν_9' vibrational wavenumbers were included without changes. The PGOPHER simulated vibronic spectrum predicts a long progression in the ν_1' butterfly mode, as well as analogous progressions of ν_1' in combination with the fundamentals of the other excited-state vibrations.
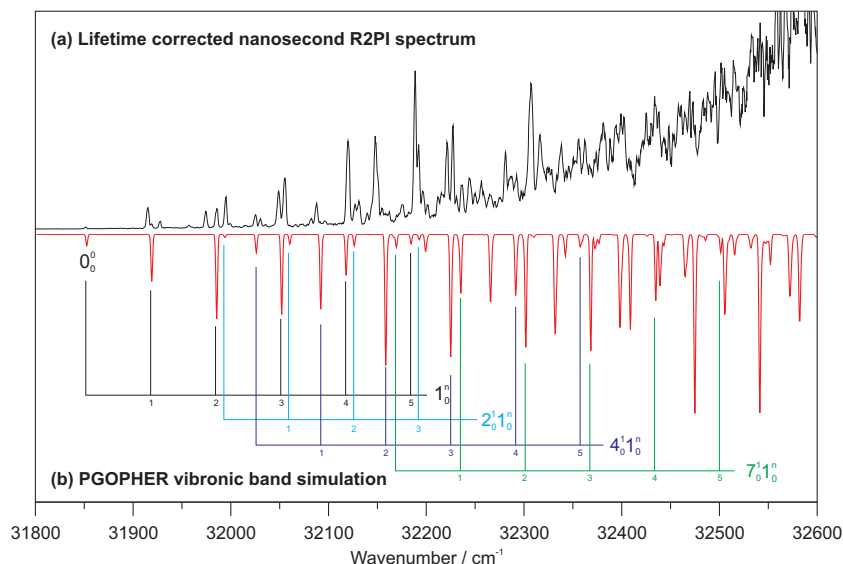
21

FIG. 10. (a) Lifetime corrected nanosecond resonant-two photon ionization spectrum of 1MCyt, see also Fig. 8 and (b) simulated vibronic spectrum (with PGOPHER, plotted in the negative direction) based on the SCS-CC2/aug-cc-pVDZ ground and $^1\pi\pi^*$ state calculations.

The latter exhibit small Franck-Condon factors. Note that the methyl rotor transitions cannot be predicted with PGOPHER. Table VI summarizes the band assignments, which are tentative, especially as regards the methyl rotor transitions.

TABLE VI. S_1 vibronic frequencies (in cm^{-1}) of 1-methylcytosine and assignments.[a]

Assignment	Frequency	Rel.intensity[b]
0_0^0	(31852.2)	1.0
1_0^1 (butterfly) + methyl rotor	64	10.8
	67	2.5
	75	3.8
1_0^2 + methyl rotor	105	2.0
	123	9.0
	134	10.3
2_0^1	143	16.0
4_0^1	173	7.3
1_0^3 + methyl rotor	179	5.3
	197	19.0
$2_0^1+1_0^1$	204	25.5
$4_0^1+1_0^1$ + methyl rotor	236	13.0
1_0^4 + methyl rotor	268	43.0
	275	13.0
	279	13.1

[a] Detailed assignments of the ν_1' (butterfly) and methyl-rotor transitions not possible, since the two modes are coupled, see the text.

[b] Relative to the 0_0^0 transition.

H. Rotational Band Contours

In the S_0 state, 1MCyt is an effectively planar asymmetric rotor: the a and b inertial axes lie in the pyrimidinone plane, as shown in Figure 11, and the c-axis is perpendicular to this plane.
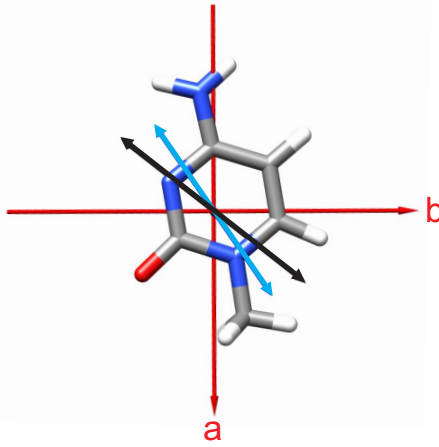
FIG. 11. SCS-CC2/aug-cc-pVDZ calculated (light blue) and experimental (black) transition dipole moment (TDM) vectors of the $S_0 \rightarrow S_1(^1\pi\pi^*)$ transition of 1-MCyt. The TDM calculation was done at the S_0 minimum structure. The in-plane a and b inertial axes are drawn in red.

Figure 12 shows the rotational band contours of several low-lying vibronic bands of 1MCyt and 1-d_3-MCyt. Due to vibronic band overlap above $0_0^0 + 190$ cm^{-1} the rotational contours can no longer be uniquely separated. The contours in Figure 12 exhibit a double-wing shape with a central dip that is characteristic for a/b-hybrid bands, which implies that the vibronic transitions are polarized in-plane. This confirms the computational predictions that the $S_0 \rightarrow S_1$ state is a $\pi\pi^*$ transition. The 0_0^0 and $0_0^0 + 64$ cm^{-1} bands of 1MCyt show an additional sharp peak just below the central dip between the wings. This peak is less pronounced in the contours of the $0_0^0 + 123$ cm^{-1} and $0_0^0 + 134$ cm^{-1} bands, which indicates a small c-type (out-of-plane) contribution to the transition dipole moment (TDM). In fact, while the MS-CASPT2 transition dipole moment along the c-axis is zero at the FC geometry, it has a clear non-zero component at the $(\pi\pi^*)_{Min}$ geometry, which we take as a further indication that the S_1 minimum is non-planar.

Rotational contour simulations for the 0_0^0+64 cm^{-1} band of 1MCyt were performed using the PGOPHER[67] program and an asymmetric rigid-rotor Hamiltonian. The SCS-CC2 ground-state A'', B'' and C'' constants given in Table VII were used as fixed inputs. The SCS-CC2 calculated changes of the rotational constants, $A' - A''$, $B' - B''$ and $C' - C''$, and the transition dipole moment (TDM) components μ_a, μ_b and μ_c were used to initiate the fitting routine. For the laser lineshape we employed a Gaussian with the measured full width at half maximum $\Delta_{Gauss} = 1.6$ GHz, see Section II B. The excited-state lifetime τ of 1MCyt contributes a

Lorentzian line shape of width $\Delta_{Lorentz} = 1/(2\pi\tau)$ to every rovibronic line, which has to be convoluted with the laser line width $\Delta_{Gauss} = 1.6$ GHz. We used the excited-state lifetime of $\tau=450$ ps, as determined by ps pump/delayed ionization measurements, see Section III E.
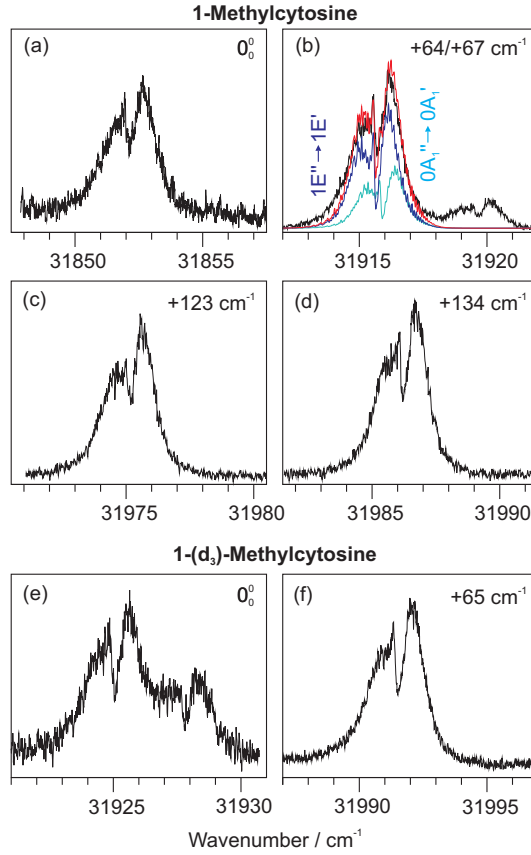

FIG. 12. Two-color R2PI rotational band contours (in black) of supersonically cooled (a)−(d) 1MCyt and (e)−(f) 1-(d_3)-MCyt with ionization at 223 nm. For the 0_0^0+64 cm^{-1} band the simulated contour is shown in red. The simulated contour exhibits a $1E'' \rightarrow 1E'$ (blue) and a $0A_1'' \rightarrow 0A_1'$ (cyan) transition, separated by 0.25 cm^{-1}.

Since the S_0 state internal-rotation levels are cooled to the lowest $0A_1''$ and $1E''$ torsional sub-levels, the vibronic bands should exhibit two torsional sub-bands corresponding to the $0A_1'' \rightarrow 0A_1'$ and $1E'' \rightarrow 1E'$ transitions. Assuming that the $0A_1'' \rightarrow 0A_1'$ excitation has only half of the intensity of the $1E'' \rightarrow 1E'$ excitation, we find that the two sub-bands cannot be separated by more than 0.25 cm^{-1}; when assuming larger sub-band splittings we were no longer able to model the double-wing shape of the contour. If we assume the SCS-CC2 calculated S_0 state barrier $V_3'' = 361$ cm^{-1} to be qualitatively correct, then the S_1 state torsional barrier V_3' has to be > 150 cm^{-1}; this is in agreement with the lowest barrier calculated on the 2D surface, see section III.F.

Although the rotational constants for the E-sub-band differ from the A-sub-band because of second-order torsion-rotation contributions,[68–71] the same parameters were used for both sub-bands. With the $0A_1'' \rightarrow 0A_1'$ transition located to by 0.25 cm^{-1} to the blue of the $1E'' \rightarrow 1E'$

TABLE VII. S_0 and $^1\pi\pi^*$ state SCS-CC2/aVDZ and B3LYP/TZVP calculated rotational constants and transition dipole moments of 1MCyt and 1-d_3-MCyt, compared to fitted values from contour simulation of the 0_0^0+64 cm^{-1} band of 1MCyt.

	1MCyt			1-(d_3)-Mcyt	
	B3LYP	SCS-CC2	0_0^0+64 cm^{-1}	B3LYP	SCS-CC2
A" (MHz)	3334.6	3276.3		3232.7	3175.8
B" (MHz)	1423.9	1398.4		1323.6	1300.9
C" (MHz)	1004.1	986.8		950.3	34.3
A'–A" (MHz)	-61.0	-89.7	-99.0	-57.9	-87.1
B'–B" (MHz)	-10.6	-14.8	18.4	-10.3	-14.0
C'–C" (MHz)	-10.3	-1.4	-13.0	-9.9	-1.3
$\|\mu_a\|:\|\mu_b\|:\|\mu_c\|$ (abs.)[a]	59:40:1	59:40:1	44:56:0	60:39:1	61:39:1
$\|\mu_a\|:\|\mu_b\|:\|\mu_c\|$ (emission) [b]	46:52:2	51:47:2		47:51:2	52:46:2

[a] Sum of transition dipole moment components normalized to 100%, using the S_0 state geometry.
[b] Sum of transition dipole moment components normalized to 100%, using the $^1\pi\pi^*$ state geometry.

sub-band, first the rotational constant changes $A' - A''$, $B' - B''$ and $C' - C''$ and then the TDM components were fitted. Figure 12(b) shows the fitted rotational contour in red, with the A- and E-sub-bands in blue. The fitted parameters are summarized in Table VII. For a good agreement with the experimental contour, the μ_b contribution had to be increased from 40% to 56%, hence the TDM vector is rotated towards the b inertial axis. However, the slow rise on the left side of the experimental contour could not be simulated.

I.   Radiationless Decay Mechanisms

To understand the radiationless decay mechanisms we have calculated the MS-CASPT2//CASSCF energy profiles for the paths to $(Eth)_X$ and $(OP)_X$, see also Section II A. The decay through $(n_O, \pi*)_X$ has not been considered because it is energetically disfavored for Cyt at the MS-CASPT2 level,[24,32] and it can be expected that 1-methyl substitution will not change this feature. The path to $(Eth)_X$ is shown in Figure 13(a). $(Eth)_X$ is similar to the structure optimized at the MS-CASPT2 level in Ref. 36 and to the analogues optimized for cytosine at different levels of theory.[21–26,30–32] Its relative energy is 31375 cm^{-1}. It is characterized by a twisted C_5-C_6 bond, with a bond length of 1.468 Å and a H-C_5-C_6-H dihedral angle of $122°$. The estimated barrier to $(Eth)_X$ is 366 cm^{-1}, which is in good agreement with the experimental break-off of vibrational structure observed at approximately 500 cm^{-1} above the 0_0^0 transition. Our estimate is based on an MS-CASPT2 single-point calculation on the CASSCF optimized transition structure and improves previous estimates (1700 - 3100 cm^{-1}) based on linear interpolations.[35,36] The orbitals involved in the excitation at $(Eth)_X$ are mainly localized on the C_5 and C_6 atoms, and the dominant configurations of the intersecting states are $(p_5)^2 (p_6)^0$ and $(p_5)^1 (p_6)^1$, see the orbitals

in Figure 13(a). In contrast, at $(^1\pi\pi^*)_{Min}$ the orbitals involved in the $S_0 \to S_1$ excitation are delocalized over the conjugated system. This suggests that the small barrier needed to access the CI is arises from the change of the wave function along the path, i.e., the localization of the excitation on the C_5-C_6 bond.
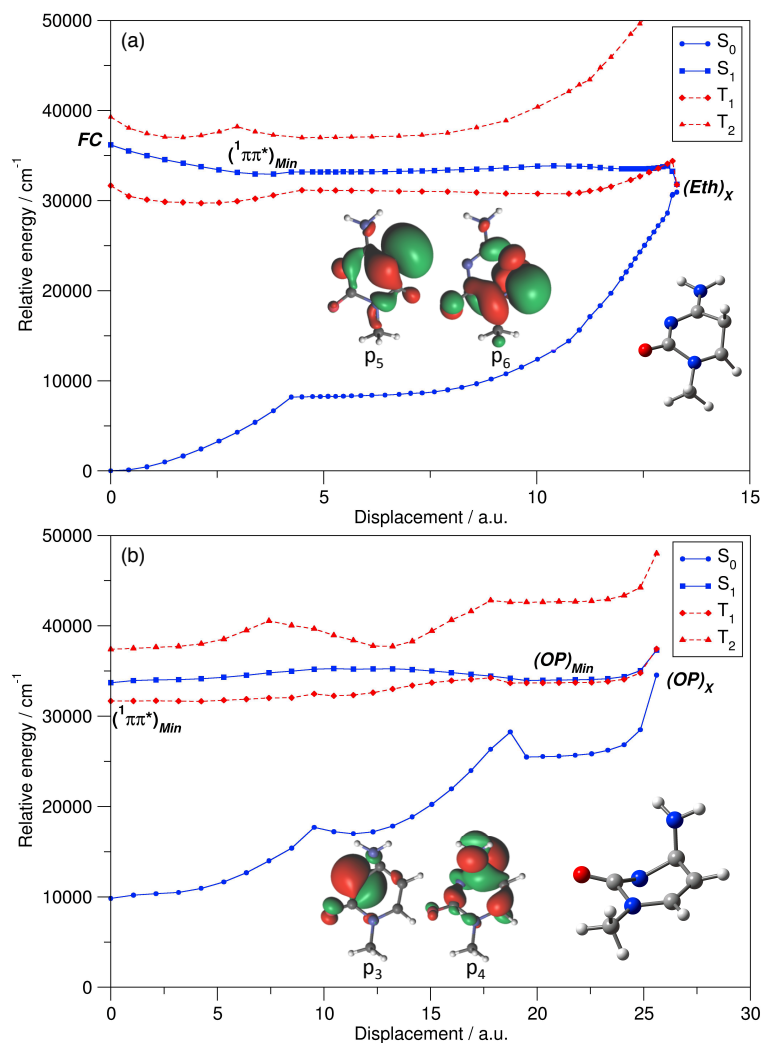

FIG. 13. MS-CASPT2 energy profile of lowest singlet and triplet states along the CASSCF optimized paths for radiationless decay on S_1. (a) From the FC structure to $(Eth)_X$ through $(^1\pi\pi^*)_{Min}$. (b) From $(^1\pi\pi^*)_{Min}$ to $(OP)_X$ through $(OP)_{Min}$. Blue circles: S_0; blue squares: S_1; red diamonds: T_1; red triangles: T_2. Insets: structure of the CI and orbitals involved in the excitation. Dominant electronic configurations at the intersections are given in the text.

The alternative decay path goes through $(OP)_X$, see Figure 13(b). At this CI, the ring

is puckered, with the N_3 ring atom and the amino group bent out of the plane (N_3-C_4-C_5-C_6 and N_8-C_4-C_5-C_6 dihedrals of $27°$ and $105°$, respectively). The decay path from $(^1\pi\pi^*)_{Min}$ to $(OP)_X$ compares well with the analogous path described for unsubstituted cytosine.[18,24–26,30,32] It involves a TS with a barrier of 934 cm^{-1} that leads to another minimum, $^1(OP)_{Min}$, with a relative energy of 242 cm^{-1} relative to $(^1\pi\pi^*)_{Min}$. The S_1/S_0 energy gap at $^1(OP)_{Min}$ is only 8469 cm^{-1}, and the decay path continues to $(OP)_X$, which lies at 35972 cm^{-1}. Similar to $(Eth)_X$, the excitation is localized on the N_3-C_4 bond (orbitals in the inset of Figure 13(b). The configurations of the intersecting states are $(p_3)^2$ $(p_4)^0$ and $(p_3)^1$ $(p_4)^1$. $(OP)_X$ is part of an extended seam[72] along the N_1 pyramidalization coordinate.

J.   Triplet State Formation and Decay

To explain the formation of the triplet state observed experimentally, we have investigated possible mechanisms for intersystem crossing (ISC) to the triplet state after excitation to the lowest-energy bands of the spectrum. At $(^1\pi\pi^*)_{Min}$, the triplet T_1 and T_2 states lie approximately 3100 cm^{-1} below and 5400 cm^{-1} above S_1, respectively. T_1 and T_2 have $\pi\pi^*$ and $n\pi^*$ character, respectively, and the calculated spin-orbit coupling (SOC) constants with S_1 are 2.4 and 10.6 cm^{-1}. This is in agreement with El-Sayed's rules,[73] which predict higher spin-orbit coupling between states with different orbital configurations (S_1 and T_2 in this case). However, ISC to T_2 is unlikely because the minimum of this state, optimized with TD-CAM-B3LYP/6-311G**, lies ~ 3100 cm^{-1} above $(^1\pi\pi^*)_{Min}$ at the MS-CASPT2 level. In contrast, the T_1 minimum, which has a semi-planar structure with a small pyramidalization at C_6, lies approximately 3100 cm^{-1} below $(^1\pi\pi^*)_{Min}$ (see Table II). Therefore, the most likely mechanism for ISC from $(^1\pi\pi^*)_{Min}$ at low excitation energies involves population of the vibrationally excited levels of T_1, similar to what was recently proposed for Cyt.[17]

We have also calculated the triplet energies along the singlet decay paths (dotted lines in Figures 13(a,b)). The S_1/T_1 energy gap remains small along both paths, ≤ 3000 cm^{-1}. This suggests that ISC is also possible at higher excitation energies, either along the decay paths to the ground state or by $S_1 \rightsquigarrow T_2$ interconversion. ISC at higher excitation energies has also been observed in mixed quantum-classical dynamics calculations for Cyt.[38] Finally, decay of T_1 can take place at a region of degeneracy with S_0. The optimized S_0/T_1 crossing structure is highly twisted along the C_5-C_6 bond (H-C_5-C_5-H dihedral of $136°$) and has an energy of 33500 cm^{-1}, and the calculated SOC element is 2.1 cm^{-1}. The relatively high energy of the crossing explains the long life time of the triplet.

IV. CONCLUSION

Our joint experimental and computational study has allowed us to interpret the R2PI spectrum of 1MCyt and provides detailed insights into the mechanisms of radiationless decay and triplet formation at low excitation energies. The lowest peak of the R2PI spectrum at 31852 cm^{-1} is assigned as the electronic origin of the spectrum. This band was assigned as a hot band in the previous study of de Vries and co-workers[9], but this explanation is excluded by the current UV/UV holeburning experiments. The calculations indicate that the S_1 minimum has a ring-puckered structure, and the large distortion upon excitation explains the low intensity of the 0_0^0 band.

Upon excitation, the ring puckering is coupled with rotation of the methyl group. This explains the difficulty to simulate the vibronic transitions that are associated with the methyl-rotation mode. For the other modes, the simulated vibronic spectrum predicts a long progression in the ν_1' butterfly vibration plus analogous progressions of ν_1' in combination with the out-of-plane ν_2', ν_4', ν_5', ν_7' and ν_9' excited-state fundamentals, in good agreement with the observed spectrum.

The R2PI spectrum breaks off after approximately 500 cm^{-1} vibrational excess energy. The calculations give two possible decay paths with low barriers which involve the ethylene and out-of-plane intersections which are well-known from the literature for cytosine. The lowest-energy path leads to the ethylene-type intersection, with a twisted C$_5$-C$_6$ bond, and has a calculated barrier of 366 cm^{-1}. The alternative path involving puckering of N$_3$ and out-of-plane bending of the amino group has an estimated barrier of 934 cm^{-1}. The good agreement between the experimental and theoretical barrier estimates is a clear indication that, at low vibrational excitation energies, the decay will involve the ethylenic intersection, similar to what has been suggested earlier for Cyt.[21–25,31,32]

The persistence of the R2PI spectrum after 30 ns delayed ionization shows that the triplet state is formed after excitation to the low energy part of the spectrum, and that intersystem crossing to the triplet is the favored decay mechanism at excitation energies below the threshold to the conical intersection. The preferred mechanism under these conditions is ISC to the vibrationally excited levels of T_1. Overall, the main effect of methyl substitution at N$_1$ on the R2PI spectrum compared to Cyt is a higher density of bands. This is similar to what is found for 5-MCyt.[74] The break-off of the spectrum is observed at similar excess energies than for Cyt and 5-MCyt, and the mechanism for triplet state formation is similar to the one found for Cyt.

Supplementary Material

See supplementary material for the synthesis of 1-methylcytosine and d_3-1-methylcytosine, additional computational details, details of UV/UV depletion spectra, delayed ionization spectra, and calculated methyl group internal rotation potentials.

Acknowledgments

---

[*] E-mail: lluis.blancafort@udg.edu

[†] E-mail: leutwyler@dcb.unibe.ch

[1] G. Fogarasi, J. Phys. Chem. A **106**, 1381 (2002).

[2] S. A. Trygubenko, T. V. Bogdan, M. Rueda, M. Orozco, F. J. Luque, J. Sponer, P. Slavicek, and P. Hobza, Phys. Chem. Chem. Phys. **4**, 4192 (2002).

[3] S. Grimme, J. Comput. Chem. **25**, 1463 (2004).

[4] Z. Yang and M. T. Rodgers, Phys. Chem. Chem. Phys. **6**, 2749 (2004).

[5] J. K. Wolken, C. Yao, F. Turećek, M. J. Polce, and C. Wesdemiotis, Int. J. Mass Spec. **267**, 30 (2007).

[6] R. Kobayashi, J. Phys. Chem. A **102**, 10813 (1998).

[7] O. Kostko, K. Bravaya, A. Krylov, and M. Ahmed, Phys. Chem. Chem. Phys. **12**, 2860 (2010).

[8] S. Lobsiger, M. A. Trachsel, H. M. Frey, and S. Leutwyler, J. Phys. Chem. B **117**, 6106 (2013).

[9] E. Nir, M. Müller, L. I. Grace, and M. S. de Vries, Chem. Phys. Lett. **355**, 59 (2002).

[10] E. Nir, I. Hünig, K. Kleinermanns, and M. S. de Vries, Phys. Chem. Chem. Phys. **5**, 4780 (2003).

[11] S. Ullrich, T. Schultz, M. Z. Zgierski, and A. Stolow, Phys. Chem. Chem. Phys. **6**, 2796 (2004).

[12] C. Canuel, M. Mons, F. Piuzzi, B. Tardivel, I. Dimicoli, and M. Elhanine, J. Chem. Phys. **122**, 074316 (2005).

[13] K. Kosma, C. Schröter, E. Samoylova, I. V. Hertel, and T. Schultz, J. Am. Chem. Soc **131**, 16939 (2009).

[14] J. W. Ho, H.-C. Yen, W.-K. Chou, C.-N. Weng, L.-H. Cheng, H.-Q. Shi, S.-H. Lai, and P.-Y. Cheng, J. Phys. Chem. A **115**, 8406 (2011).

[15] S. Blaser, M. A. Trachsel, S. Lobsiger, T. Wiedmer, H.-M. Frey, and S. Leutwyler, J. Phys. Chem. Lett. **7**, 752 (2016).

[16] S. Lobsiger and S. Leutwyler, J. Phys. Chem. Lett. **3**, 3576 (2012).

[17] S. Lobsiger, M. Etinski, S. Blaser, H.-M. Frey, C. Marian, and S. Leutwyler, J. Chem. Phys. **143**, 234301 (2015).

[18] N. Ismail, L. Blancafort, M. Olivucci, B. Kohler, and M. Robb, J. Am. Chem. Soc. **124**, 6818 (2002).

[19] M. Merchán and L. Serrano-Andrés, J. Am. Chem. Soc. **125**, 8108 (2003).

[20] L. Blancafort and M. A. Robb, J. Phys. Chem. A **108**, 10609 (2004).

[21] K. Tomic, J. Tatchen, and C. M. Marian, J. Phys. Chem. A **109**, 8410 (2005).

[22] M. Z. Zgierski, S. Patchkovskii, T. Fujiwara, and E. C. Lim, J. Chem. Phys. **123**, 081101 (2005).

[23] M. Merchán, R. Gonzalez-Luque, T. Climent, L. Serrano-Andrés, E. Rodríguez, M. Reguero, and D. Peláez, J. Phys. Chem. B **110**, 26471 (2006).

[24] L. Blancafort, J. Photochem. Photobiol. **83**, 603 (2007).

[25] K. A. Kistler and S. Matsika, J. Phys. Chem. A **111**, 2650 (2007).

[26] H. R. Hudock and T. J. Martínez, Chem. Phys. Chem. **9**, 2486 (2008).

[27] K. A. Kistler and S. Matsika, J. Chem. Phys. **128**, 215102 (2008).

[28] L. Serrano-Andrés and M. Merchán, J. Photochem. Photobiol. C **10**, 21 (2009).

[29] M. Barbatti, A. J. A. Aquino, J. J. Szymczak, D. NAchtigallova, P. Hobza, and H. Lischka, Proc. Natl. Acad. Sci **107**, 21453 (2010).

[30] M. Barbatti, A. J. A. Aquino, J. J. Szymczak, D. Nachtigallova, and H. Lischka, Phys. Chem. Chem. Phys. **13**, 6145 (2011).

[31] M. Kotur, T. C. Weinacht, C. Zhou, K. A. Kistler, and S. Matsika, J. Chem. Phys. **134**, 184309 (2011).

[32] A. Nakayama, Y. Harabuchi, S. Yamazaki, and T. Taketsugu, Phys. Chem. Chem. Phys. **15**, 12322 (2013).

[33] F. J. Avila Ferrer, F. Santoro, and R. Improta, Comput. Theor. Chem. **1040**, 186 (2014).

[34] R. Improta, F. Santoro, and L. Blancafort, Chem. Rev. **116**, 3540 (2016).

[35] Q. S. Li and L. Blancafort, Photochem. Photobiol. Science **12**, 1401 (2013).

[36] A. Nakayama, S. Yamazaki, and T. Taketsugu, J. Phys. Chem. A **118**, 9429 (2014).

[37] M. Merchán, L. Serrano-Andrés, M. A. Robb, and L. Blancafort, J. Am. Chem. Soc. **127**, 1820 (2005).

[38] M. Richter, P. Marquetand, J. Gonzalez-Vazquez, I. Sola, and L. Gonzalez, J. Phys. Chem. Letters **3**, 3090 (2012).

[39] N. Forsberg and P. A. Malmqvist, Chem. Phys. Lett. **274**, 196 (1997).

[40] G. Ghigo, B. O. Roos, and P. A. Malmqvist, Chem. Phys. Lett. **396**, 142 (2004).

[41] C. González and H. B. Schlegel, J. Phys. Chem. **94**, 5523 (1990).

[42] P. Celani, M. A. Robb, M. Garavelli, F. Bernardi, and M. Olivucci, Chem. Phys. Lett. **243**, 1 (1995).

[43] S. Ruiz-Barragan, M. A. Robb, and L. Blancafort, J. Chem. Theory Comput. **9**, 1433 (2013).

[44] TURBOMOLE *V6.4 2013* (A Development of Universität Karlsruhe (TH) and Forschungszentrum Karlsruhe GmbH, 1989-2007, TURBOMOLE GmbH; available from `http://www.turbomole.com`. (accessed May 19, 2015)).

[45] "The thresholds for scf and one-electron density convergence were set to 10^{-9} a.u. and 10^{-8} a.u., respectively. the convergence thresholds for all structure optimizations were set to 10^{-8} a.u. for the energy change, $6 \cdot 10^{-6}$ a.u. for the maximum displacement element, 10^{-6} a.u. for the maximum gradient element, $4 \cdot 10^{-6}$ a.u. for the rms displacement and 10^{-6} a.u. for the rms gradient.".

[46] M. J. Frisch, G. W. Trucks, H. B. Schlegel, G. E. Scuseria, M. A. Robb, J. R. Cheeseman, G. Scalmani, V. Barone, B. Mennucci, G. A. Petersson, and et al, "Gaussian 09 Revision A.02," (2009), Gaussian, Inc., Wallingford CT, 2009.

[47] G. Karlstrom, R. Lindh, P. A. Malmqvist, B. O. Roos, U. Ryde, V. Veryazov, P. O. Widmark, M. Cossi, B. Schimmelpfennig, P. Neogrady, and L. Seijo, Comput. Mat. Sci. **28**, 222 (2003).

[48] F. Aquilante, L. De Vico, N. Ferré, G. Ghigo, P.-A. Malmqvist, P. Neogrady, T. B. Pedersen, M. Pitonak, M. Reiher, B. O. Roos, L. Serrano-Andrés, M. Urban, V. Veryazov, and R. Lindh, Journal of Computational Chemistry **31**, 224 (2010).

[49] T. J. Kistenmacher, M. Rossi, J. Caradonna, and L. G. Marzilli, Adv. Mol. Rel. Int. Proc. **15**, 119 (1979).

[50] S. Lobsiger, H. M. Frey, and S. Leutwyler, Phys. Chem. Chem. Phys. **12**, 5032 (2010).

[51] S. Blaser, H.-M. Frey, C. G. Heid, and S. Leutwyler, Chimia **86**, 260 (2014).

[52] S. Lobsiger, R. K. Sinha, S. Blaser, H.-M. Frey, and S. Leutwyler, Nature Chemistry **6**, 989 (2014).

[53] (Interactive Data Language, Version 7.1, ITT Visual Information Solutions, 2009) www.ittvis.com/idl.

[54] K. A. Kistler, F. C. Spano, and S. Matsika, J. Phys. Chem. B **117**, 2032 (2013).

[55] R. Abouaf, J. Pommier, H. Dunet, P. Quan, P.-C. Nam, and M. T. Nguyen, J. Chem. Phys. **121**, 11668 (2004).

[56] O. Dolgounitcheva, V. G. Zakrzewski, and J. V. Ortiz, J. Phys. Chem. A **107**, 822 (2003).

[57] M. Liu, T. Li, F. S. Amegayibor, D. S. Cardoso, Y. Fu, and J. K. Lee, J. Org. Chem. **73**, 9283 (2008).

[58] C. Yao, M. L. Cuadrado-Peinado, M. Polášek, and F. Tureček, J. Mass Spectrom. **40**, 1417 (2005).

[59] M. Harańczyk, J. Rak, and M. Gutowski, J. Phys. Chem. A **109**, 11495 (2005).

[60] E. C. Lim and J. M. H-Hu, J. Chem. Phys. **45**, 4742 (1966).

[61] E. C. Lim, J. Phys. Chem. **90**, 6770 (1986).

[62] D. M. Close, J. Phys. Chem. A **108**, 10376 (2004), http://pubs.acs.org/doi/pdf/10.1021/jp046660y.

[63] C. Yu, S. Peng, I. Akiyima, J. Lin, and P. R. LeBreton, J. Am. Chem. Soc. **100**, 2303 (1978).

[64] D. G. Lister, J. N. Macdonald, and N. L. Owen, *Internal Rotation and Inversion - An Introduction to*

Large Amplitude Motions in Molecules (ACADEMICS PRESS INC. (LONDON) LTD, 1978).

[65] R. M. Dimeo, *Simple Quantum Visualizations Using IDL* (NIST Center for Neutron Research, 2009).

[66] I. Kleiner and J. T. Hougen, J. Phys. Chem. A **119**, 10664 (2015).

[67] C. M. Western, *PGOPHER 8.0, a Program for Simulating Rotational, Vibrational and Electronic Structure* (University of Bristol, 2015) pgopher.chm.bris.ac.uk.

[68] X.-Q. Tan, W. A. Majewski, D. F. Plusquellic, and D. W. Pratt, J. Chem. Phys. **94**, 7721 (1991).

[69] L. Alvarez-Valtierra, J. Yi, and D. W. Pratt, J. Phys. Chem. B **110**, 19914 (2006).

[70] L. Alvarez-Valtierra, X.-Q. Tan, and D. W. Pratt, J. Phys. Chem. A **111**, 12802 (2007).

[71] P. J. Morgan, L. Alvarez-Valtierra, and D. W. Pratt, J. Phys. Chem. A **113**, 13221 (2009).

[72] L. Blancafort, ChemPhysChem **15**, 3166 (2014).

[73] M. El-Sayed, Acc. Chem. Res. **1**, 8 (1968).

[74] M. A. Trachsel, S. Lobsiger, and S. Leutwyler, J. Phys. Chem. B **116**, 11081 (2012).